



N-doped $\text{ZrO}_2/\text{TiO}_2$ bimetallic materials synthesized in supercritical CO_2 : Morphology and photocatalytic activity

Rahima A. Lucky, Paul A. Charpentier*

Department of Chemical and Biochemical Engineering, University of Western Ontario, London, Ontario, Canada N6A 5B9

ARTICLE INFO

Article history:

Received 25 May 2009

Received in revised form 27 February 2010

Accepted 9 March 2010

Available online 16 March 2010

Keywords:

ZrO_2 modified TiO_2 nanostructure

Sol-gel chemistry

Supercritical carbon dioxide

Characterization

Photocatalysis

ABSTRACT

A series of N- and N/Zr-doped titanium nanomaterials were synthesized via an acetic acid modified sol-gel route using supercritical carbon dioxide (scCO_2) as both the synthesis and drying medium. Titanium isopropoxide (TIP), and triethylamine (TEA) w/wo zirconium propoxide precursors were reacted with acetic acid in a polycondensation reaction in scCO_2 . The effects of N and N/Zr doping on the morphology, phase structure, mean crystallite size, textural properties, thermal and crystallization behavior, and photocatalytic degradation of methylene blue was investigated. SEM and TEM analysis showed that pure titania formed nanofibers from TIP and acetic acid whereas the doped samples gave a flake-like structure. The SEM and TEM images showed that a porous material consisting of ca. 10–15 nm crystals were formed. XPS spectra indicated that the N_{1s} peak for both N-doped titania and Ti-Zr binary metal oxide were centered at 400 eV, indicating effective doping of nitrogen in the TiO_2 matrix. From the XRD analysis, it was observed that a small amount of nitrogen and zirconia inhibited the crystal growth, resulting in smaller crystallite materials. The BET analysis of the N_2 isotherm data revealed that small amount of zirconia and nitrogen (0.4 at%) increased the surface area. All synthesized doped samples gave superior photocatalytic degradation of methylene blue compared to P25. These results show that scCO_2 is a new promising route to provide N- and N/Zr-doped advanced photocatalytic nanomaterials.

© 2010 Elsevier B.V. All rights reserved.

1. Introduction

TiO_2 nanomaterial is a potential candidate for solar applications such as dye-sensitized solar cells (DSSCs) and next-generation photocatalytic reactors due to titania's unique optoelectronic and photochemical properties [1–3]. However, pure anatase TiO_2 activates at $\lambda < 380$ nm of UV light, leaving approximately 95% of the available solar energy unused, and shows a high recombination rate of the photogenerated electron–hole pairs [4]. In the technical literature, numerous studies have focused on shifting TiO_2 's band gap to the visible spectral region, in order to harness more of the visible light, hence, greatly expanding its application [5–8]. Through several theoretical and experimental investigations conducted by Ashai and coworkers, along with others on the effects of different non-metal doping systems in TiO_2 , N doping has been shown to be a very effective technique for band gap narrowing, resulting in visible light absorption [9–12]. In addition, Wang et al. investigated the role of the potential promoter ZrO_2 in enhancing activity of $\text{TiO}_{2-x}\text{N}_x$ for the oxidation of gaseous organic compounds [13].

* Corresponding author at: Department of Chemical and Biochemical Engineering, University of Western Ontario, Faculty of Engineering, London, Ontario, Canada N6A 5B9. Tel.: +1 519 661 3466; fax: +1 519 661 3498.

E-mail address: pcharpentier@eng.uwo.ca (P.A. Charpentier).

They reported that ZrO_2 helped to preserve the surface area and prevent grain growth resulting in higher activity. Therefore, simultaneous Zr and N doping could help to enhance the performance of TiO_2 nanomaterials for photocatalysis as Zr doping has been shown to increase the surface area and thermal stability while reducing the crystal size of the TiO_2 nanomaterials [14,15].

Most of the methods currently being used for catalyst synthesis suffer scale-up problems, and are not environmentally friendly. These include template methods, hydrothermal, solvothermal and CVD processes [16]. Recently, the sol-gel process has become an attractive synthesis route to produce high quality, homogeneous metal oxide materials with desired nanostructure at low cost [17,18] and has been used for synthesizing N-doped TiO_2 [19]. Drying of the gel with supercritical carbon dioxide (scCO_2) forms aerogels, which possess catalytically favorable textural properties with high accessible internal surface areas and excellent availability of active centers to a reactant [20]. Previously we synthesized $\text{ZrO}_2\text{-TiO}_2$ nanotubular and nanorod structures in scCO_2 , finding that it was an attractive solvent for the synthesis and processing of high quality porous materials [21]. There are several favorable physical properties such as low viscosity, “zero” surface tension and high diffusivity of scCO_2 which enable it to produce superior ultrafine and uniform nanomaterials [22,23]. In addition, scCO_2 can be removed completely from the products by venting; hence, no drying process is required and the porous structure can be maintained

without collapsing the nanostructure. Furthermore, scCO₂ can be easily recycled after the pressure is diminished for potential scale-up. Therefore, this research examines the synthesis of TiO₂ based nanomaterials by simultaneous zirconium and nitrogen doping via the sol-gel process in scCO₂. The morphology, crystal structure, crystal size, surface area, pore volume and pore size distribution of the synthesized nanomaterials were examined, along with characterizing their photocatalytic ability using the model compound methylene blue, showing the materials provided superior photocatalytic ability compared to the standard titania photocatalyst (Degussa P25).

2. Experimental

2.1. Materials

Reagent grade titanium (IV) isopropoxide (TIP, 97%, Aldrich), zirconium (IV) propoxide (ZPO, 70%, Aldrich), acetic acid (99.7%, Aldrich), isopropanol (99.5%, Aldrich), triethylamine (TEA, 99.7%, Aldrich), and instrument grade carbon dioxide (99.99%, BOC) were used without further purification.

2.2. Synthesis

Both N- and N/Zr-doped TiO₂ nanomaterials were synthesized following the standard procedure previously provided [21] using TIP, ZPO and TEA. In a typical experiment, 6.6 mmol TIP, 0.4 mmol ZPO, 35 mmol acetic acid and the appropriate amount of TEA were quickly placed in a 10 mL view cell under stirring. Then CO₂ was added to the system with heating to achieve a final temperature and pressure of 60 °C and 5000 psig, respectively. Initially, a transparent homogeneous pale yellow to brown phase was observed depending on the TEA/TIP ratio. After the reaction mixture was stirred for 30 min to several hours, the fluids in the view cell became semi-transparent then turned white, indicating a phase change and gel formation. After 5 days of aging, a few droplets were vented and placed in a test tube, followed by addition of water. When a higher amount of TEA was used, white precipitate formed indicating incomplete polycondensation. However, to maintain consistency, after 5 days of aging, the nanomaterial samples were washed using CO₂ at a controlled flow rate (≈ 0.5 ml/min). As-prepared samples were taken for subsequent characterization, with the remainder calcined in air at 500 °C using a heating rate of 10 °C/min, holding time of 2 h, and cooling rate to room temperature of 0.5 °C/min. The following samples were prepared: (1) pure TiO₂, (2) Zr modified TiO₂, (3) TiO₂-N1 and TiO₂-N2, respectively, and (4) Zr-TiO₂-N1 and Zr-TiO₂-N2. The ratio of TEA/Ti precursors is 0.4 and 0.6 for sample named N1 and N2, respectively.

2.3. Characterization

Scanning electron microscopy (SEM) measurements were used to determine the size and morphology of nanomaterials using a LEO 1530 SEM. Transmission electron microscopy (TEM) and high resolution TEM (HRTEM) images were obtained using a Philips CM 10 and JOEL 2010f, respectively. The specimens were dispersed in methanol and placed on a copper grid covered with holey carbon film. Thermo-gravimetric analysis (TGA) was performed under nitrogen atmosphere on a TA Instrument TA-Q500 at a heating rate of 10 °C/min from room temperature to 800 °C. X-ray diffraction (XRD) was performed utilizing Rigaku employing CuK α 1 + K α 2 = 1.54184 Å radiation with a power of 40 kV–35 mA for the crystalline analysis. The broad-scan analysis was typically conducted within the 2 θ range of 10–80°, and the strongest peak for the anatase (1 0 1) and the rutile (1 1 0) phases of TiO₂ was used to

determine the average N-doped Zr-TiO₂ nanocrystallite size using Scherrer's equation:

$$D = \frac{0.9\lambda}{\beta \cos \theta} \quad (1)$$

where D is the average nanocrystallite size (nm), λ is the X-ray wavelength (1.541 Å), β is the full-width at half-maximum intensity (in radian), and θ is the half of diffraction peak angle.

The samples were further analyzed using a Renishaw Model 2000 Raman spectrometer equipped with a 633 nm laser. The power at the sample varied between 0.2 and 0.5 mW with the beam defocused to an area of approximately 5–10 μm in diameter. The microstructural properties such as surface area, pore volume and pore size distribution of the aerogels and the oxides was obtained using N₂ physisorption at 77 K with a Micromeritics ASAP 2010. Prior to the N₂ physisorption, the samples were degassed at 200 °C under vacuum. From the N₂ adsorption isotherms, the specific surface area was calculated. The mesopore volume (V_{BJH}), the average pore diameters (d_p), and the pore size distributions were estimated by the Barret–Joyner–Halenda (BJH) method applied to the desorption branch of the isotherm.

2.4. Photocatalytic activity

Methylene blue (MB, 0.05 wt% water solution, Sigma-Aldrich), was chosen as the model organic compound to evaluate the photoactivity of the prepared TiO₂ based nanomaterials. The catalytic performance was evaluated under UV light irradiation using a 100 W high-pressure mercury lamp (UVP, USA) with a wavelength range of 320–400 nm and peak wavelength of 365 nm. Typically, a mixture of methylene blue solution (15 μmol/L, 100 mL) and 25 mg of catalyst was vigorously stirred for 30 min to establish an adsorption/desorption equilibrium. Then the reaction solution was stirred under light irradiation. The temperature of the photocatalytic reaction was measured by thermometer and found not to deviate significantly from room temperature. At given time intervals, 3 mL aliquots were sampled and centrifuged to remove the particles. The filtrates were analyzed by measuring the absorption band maximum (665 nm) using a Cary 50 UV-vis spectrophotometer. The methylene blue concentration was calculated by using a calibration curve according to the absorbance intensity at 665 nm in the photocatalytic process. A control photodegradation experiment was also performed without catalyst, resulting in a negligible decrease in concentration (below 2%) during the 1-h irradiation period. When the experiment was carried out with catalyst but in the absence of light irradiation, no change in methylene blue concentration was observed. Repeat tests were run to ensure data reliability.

3. Results and discussion

3.1. Synthesis and morphology

The morphology and size of the as-prepared materials synthesized in supercritical carbon dioxide (scCO₂) were characterized by SEM analysis as shown in Fig. 1. The pure TiO₂ nanomaterials (Fig. 1(A)) consisted of nanofibers having 20–50 nm diameter, consistent with the previous work reported by Sui et al. [22]. The N-doped TiO₂ consists of uniform sized sheets of 200 nm width and ca. 1 μm length (Fig. 1(B)). In our previous work, we observed nanotubular structures of Zr-TiO₂ being formed in scCO₂ that we attributed to a “roll-up” mechanism [21,24]. However, here we see that Zr modified N-doped TiO₂ exhibits a flower type structure consisting of sheets ca. 500 nm width as shown in Fig. 1(C) with very thin edges. Further increasing the N concentration gave a denser nanostructure (Fig. 1(D)).

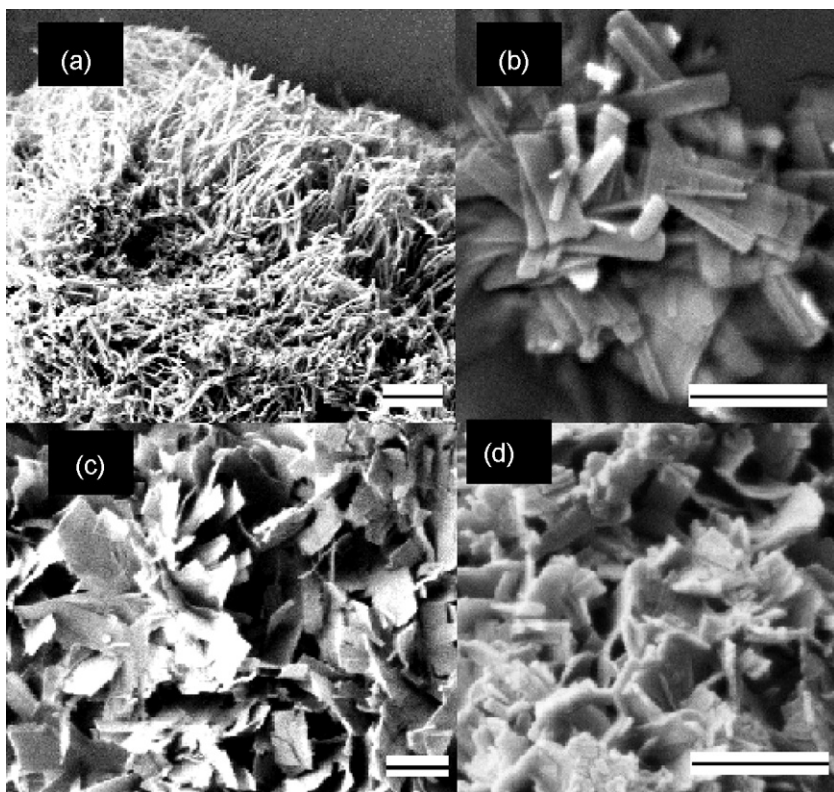


Fig. 1. SEM: (A) TiO_2 , (B) $\text{TiO}_2\text{-N}1$, (C) $\text{Zr-TiO}_2\text{-N}1$, and (D) $\text{Zr-TiO}_2\text{-N}2$. (Bar represents 500 nm. All the samples were examined after platinum coating).

TEM analysis was performed to obtain more detailed structural information on the calcined materials, with the images given in Fig. 2. It can be seen that calcined pure TiO_2 fibers have 30 nm diameters (Fig. 2(A)) whereas all N-doped samples are sheets with

100–300 nm width (Fig. 2(B–D)). The TEM images also confirmed that the doping agent had a significant effect on the crystal size and porosity of the calcined nanomaterials. The measured crystal size for all systems was ca. 10–15 nm, though the shapes of

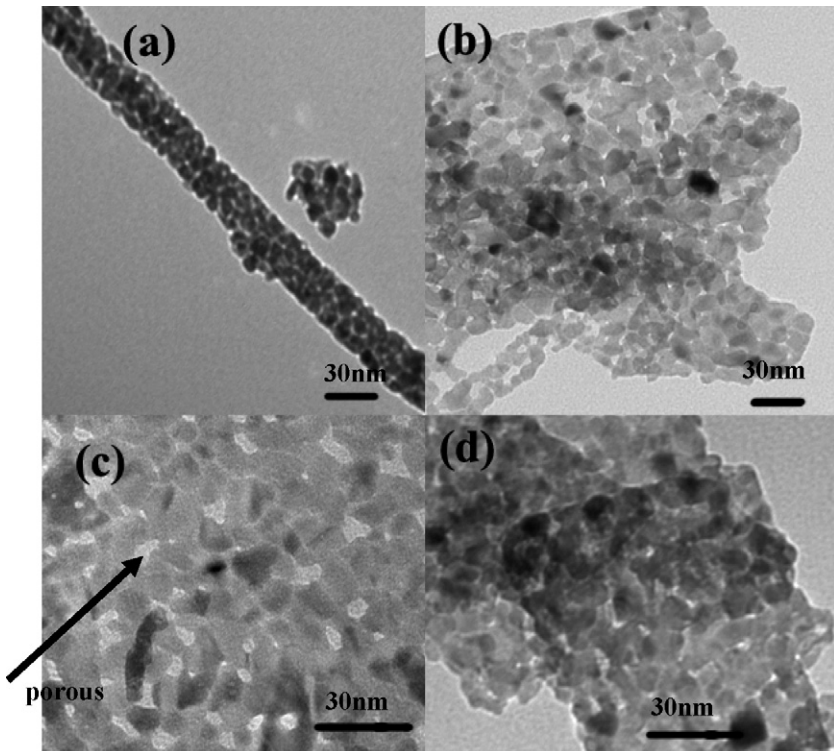


Fig. 2. TEM: (A) TiO_2 , (B) $\text{TiO}_2\text{-N}1$, (C) $\text{Zr-TiO}_2\text{-N}1$, and (D) $\text{TiO}_2\text{-N}2$. (Bar represents 30 nm).

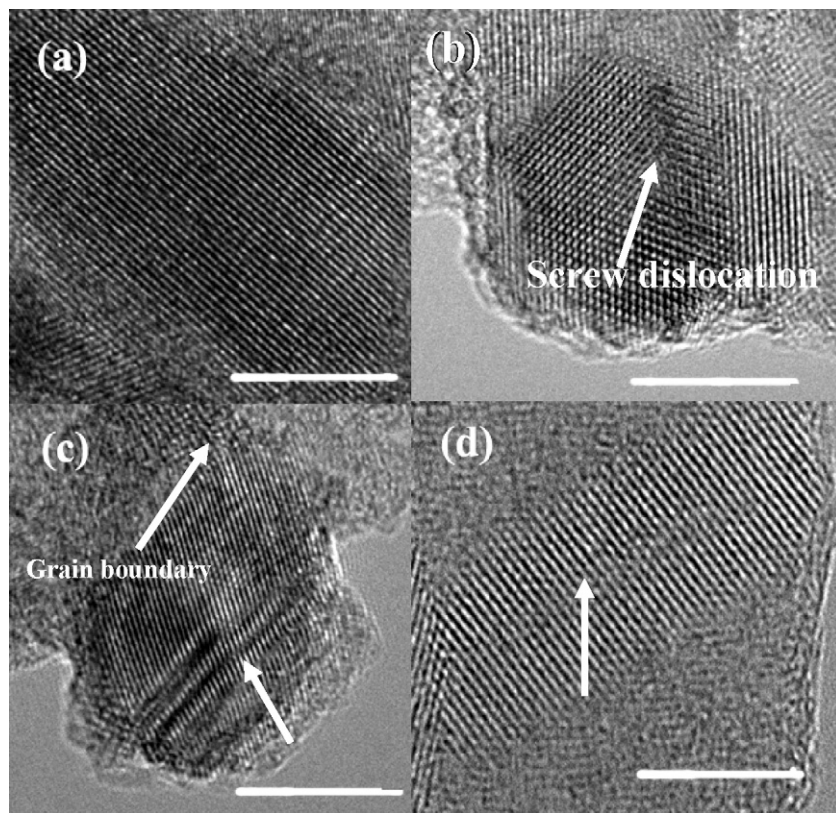


Fig. 3. HRTEM for N-doped TiO_2 nanomaterials: (A) TiO_2 , (B) $\text{TiO}_2\text{-N1}$, (C) $\text{Zr-TiO}_2\text{-N1}$, and (D) $\text{TiO}_2\text{-N2}$. (Bar represents 5 nm. Arrows indicate defects).

the crystallites are different. Pure TiO_2 formed nice cubic crystals whereas in the modified system, poorer crystallinity was observed. It is known that the Zr and N present in the samples retards the reorganization for forming ordered crystal structures, resulting in poor crystallinity for the modified systems [25,26]. Similar to the SEM results, the TEM images also confirm that the materials were very solid (less porous) when a higher amount of triethylamine was used.

To explore the crystal structure in more detail, HRTEM analysis for both the pure TiO_2 and the modified samples calcined at 500 °C was performed. The HRTEM micrographs for the pure TiO_2 in Fig. 3(A) demonstrate long grains having the anatase crystal phase with a d -spacing 0.35 nm. This d -spacing value is assigned to the lattice spacing of the (1 0 1) planes of the anatase phase. Upon introducing dopant into the TiO_2 matrix, the crystallites became smaller. However, the HRTEM analysis further reveals that the N-doped systems (Fig. 3(B–D)) have many defects (grain boundary, lattice mismatch, screw dislocation), which may be due to the presence of alkylamine in the synthesis process. Alkylamines can be selectively adsorbed on certain crystal facets of metal oxides, or form amine complexes with metal alkoxides, thus leading to orientated growth or aggregation of the metal oxide particles [27,28].

TG-DTG analysis was carried out to study the thermal decomposition behavior of the synthesized nanomaterials, in order to confirm the proper calcination temperature to provide crystal structure. The TG curves given in Fig. 4(A) along with the DTG curves (Fig. 4(B)) show three regions of weight loss in the range 25–125, 125–500 and above 500 °C. Usually, the first stage of weight loss is attributed to the removal of physically adsorbed organics and water, while the second range is mainly attributed to the removal of coordinated organic material, i.e. acetic acid [29,30]. In the first stage, all samples similarly lost ca. 4–5 wt%, however, a significant difference in weight loss is observed in the second stage for the studied samples. The pure TiO_2 sample lost 51 wt% in the second

stage, whereas N-doped TiO_2 lost 55 wt%. However, upon introducing 6% Zr into the matrix, the samples became more condensed compared to TiO_2 as previously observed by SEM, and only 50% weight loss was found during this stage. Moreover, when N was introduced into the $\text{ZrO}_2\text{-TiO}_2$ system through TEA, the weight loss was lower compared to the N-doped TiO_2 , i.e. 51%. The DTG curves presented in Fig. 4(B) clearly show the effects of dopant on the removal of organic residue by heat treatment. The peak position (Fig. 4(B)(b) and (d)) shifted to lower values compared to pure TiO_2 (Fig. 4(B)(a)) after introducing triethylamine, regardless of Zr modification, indicating easy removal of the residue. However, the opposite phenomenon was observed for zirconia doping, where the Zr cation shifted the peak positions to a higher value (Fig. 4(B)(c)) indicating higher thermal stability. Higher thermal stability is a well known property of ZrO_2 , which has been observed in many systems [31]. The weight loss over 500 °C was extremely small for all samples showing that 500 °C is a reasonable calcination temperature for these samples. Hence, this analysis shows that the studied dopants have a very prominent effect on the decomposition or removal of the organic residue.

3.2. XRD analysis

The crystal structure and crystallite size of the nanomaterials calcined at 500 °C were examined by XRD, with the spectra given in Fig. 5. This figure shows that all modified calcined nanomaterials consist of anatase crystal, although the peak intensity as well as the FWHM strongly depends on the type and amount of dopant. The pure TiO_2 (Fig. 5(a)) showed a very small rutile phase (4 wt%) at this temperature. For Fig. 5(d–f), no distinct ZrO_2 or in the N containing samples (b, c, e, f) no TiN peak is evident, indicating no phase separation, and that the dopant was contained in the anatase crystal structure for this composition.

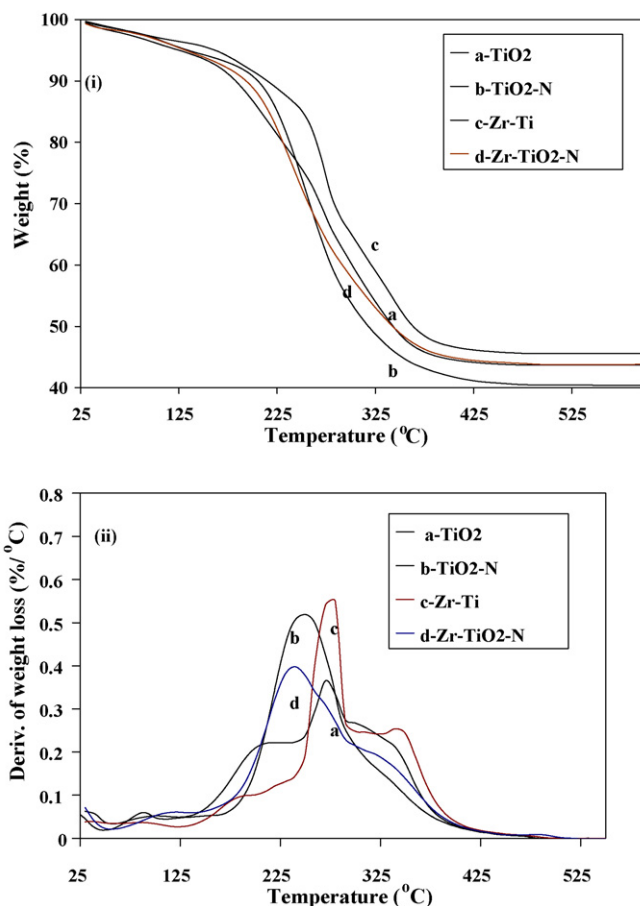


Fig. 4. Thermal decomposition behavior of N-doped nanomaterials as a function of temperature: (A) TG and (B) DTG.

The crystallite sizes for the various synthesized samples were calculated using Scherer's equation from the XRD data (Eq. (1) in Section 2), and are given in Table 1. It can be seen that the crystal size for pure TiO_2 calcined at 500 °C was ca. 13.8 nm, whereas $\text{TiO}_2\text{-N}1$ had 12.9 nm crystallites with a higher amount of TEA ($\text{TiO}_2\text{-N}2$) further reducing the crystallite size to 8.7 nm. The Zr modified nanomaterials had smaller crystallites compared to the unmodified samples, regardless of the amount of TEA used. Moreover, TEA reduced the crystallinity of the modified samples compared to unmodified samples decreasing Zr-TiO_2 from 12.3 to 11.1 nm for $\text{Zr-TiO}_2\text{-N}1$ and 6.2 nm for $\text{Zr-TiO}_2\text{-N}2$. These results are consistent with those obtained from the TEM analysis. The dopant prevents rearrangement of atoms to form crystal, hence lowering crystallinity and giving smaller size crystallites [26].

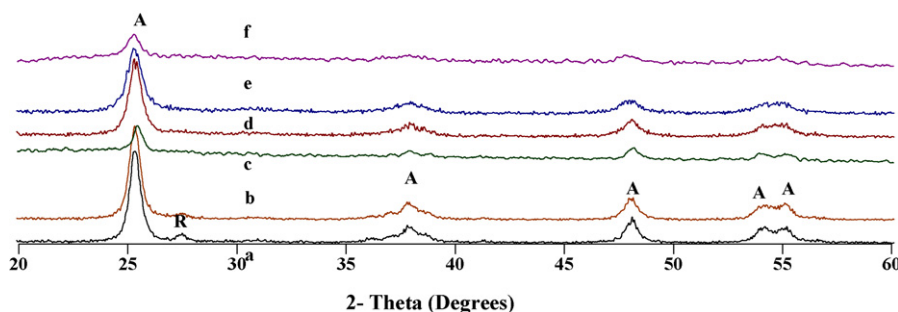


Fig. 5. Powder XRD spectra of the Zr modified N-doped TiO_2 nanomaterials calcined at 500 °C: (a) TiO_2 , (b) $\text{TiO}_2\text{-N}1$, (c) $\text{TiO}_2\text{-N}2$, (d) Zr-TiO_2 , (e) $\text{Zr-TiO}_2\text{-N}1$, and (f) $\text{Zr-TiO}_2\text{-N}2$. (A-anatase, R-rutile).

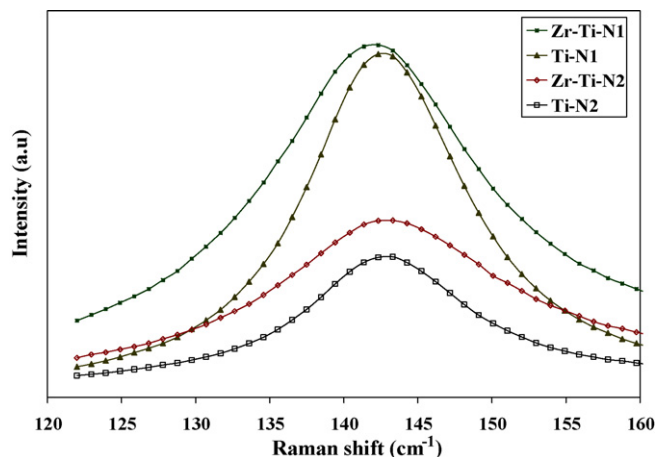


Fig. 6. Raman spectra around 142 cm^{-1} for Zr modified N-doped TiO_2 nanomaterials calcined at 500 °C.

3.3. Raman

To further verify these results, Raman analysis was performed on all the N-doped samples. The spectra for the calcined samples show Raman peaks at 142 , 395 , 517 and 639 cm^{-1} that can be assigned to the E_g , B_{1g} , B_{1g}/A_{1g} , E_g , modes of the anatase of titania, respectively, which agrees with published values [32]. However, the most intense anatase peak at $\approx 142 \text{ cm}^{-1}$ showed significant differences amongst the different samples (Fig. 6). The Raman peaks usually display smaller linewidths (FWHM) for larger crystallites due to an increase in the correlation length of the vibrations, with increasing intensity indicating greater concentrations of anatase phase [33]. The FWHM of the anatase peak were ca. 11 cm^{-1} for both the Ti and Zr-Ti systems modified with a lower amount of triethylamine. However, this value increased to ca. 15 cm^{-1} for samples prepared using a higher amount of TEA. More importantly, the Raman peak intensity reduced to half compared to the previous system, indicating lower crystallinity. Moreover, the peaks shifted to higher frequencies, also confirming smaller crystallite sizes were formed.

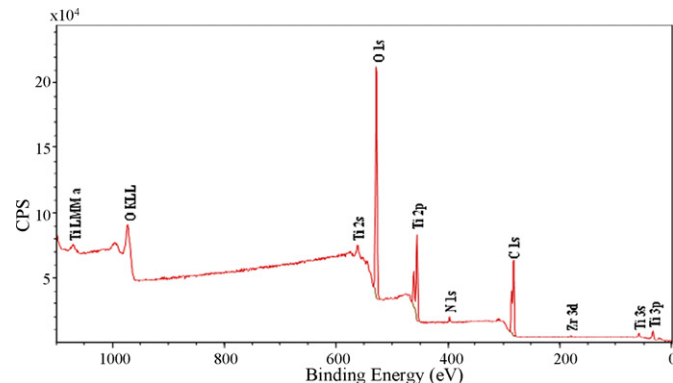
3.4. XPS analysis

Fig. 7 shows a typical XPS spectrum for the Zr modified N-doped TiO_2 nanomaterials synthesized by the sol-gel process in scCO_2 . XPS peaks show that the $\text{Zr-TiO}_2\text{-N}$ powder contains Ti, Zr, O, N, and C elements. The presence of carbon is ascribed to the residual carbon from the precursor solution, and any adventitious hydrocarbon from the XPS instrument itself. This XPS data reveals that the Zr and N elements are incorporated into the TiO_2 crystal lattice, or were adsorbed onto the surface of the crystals.

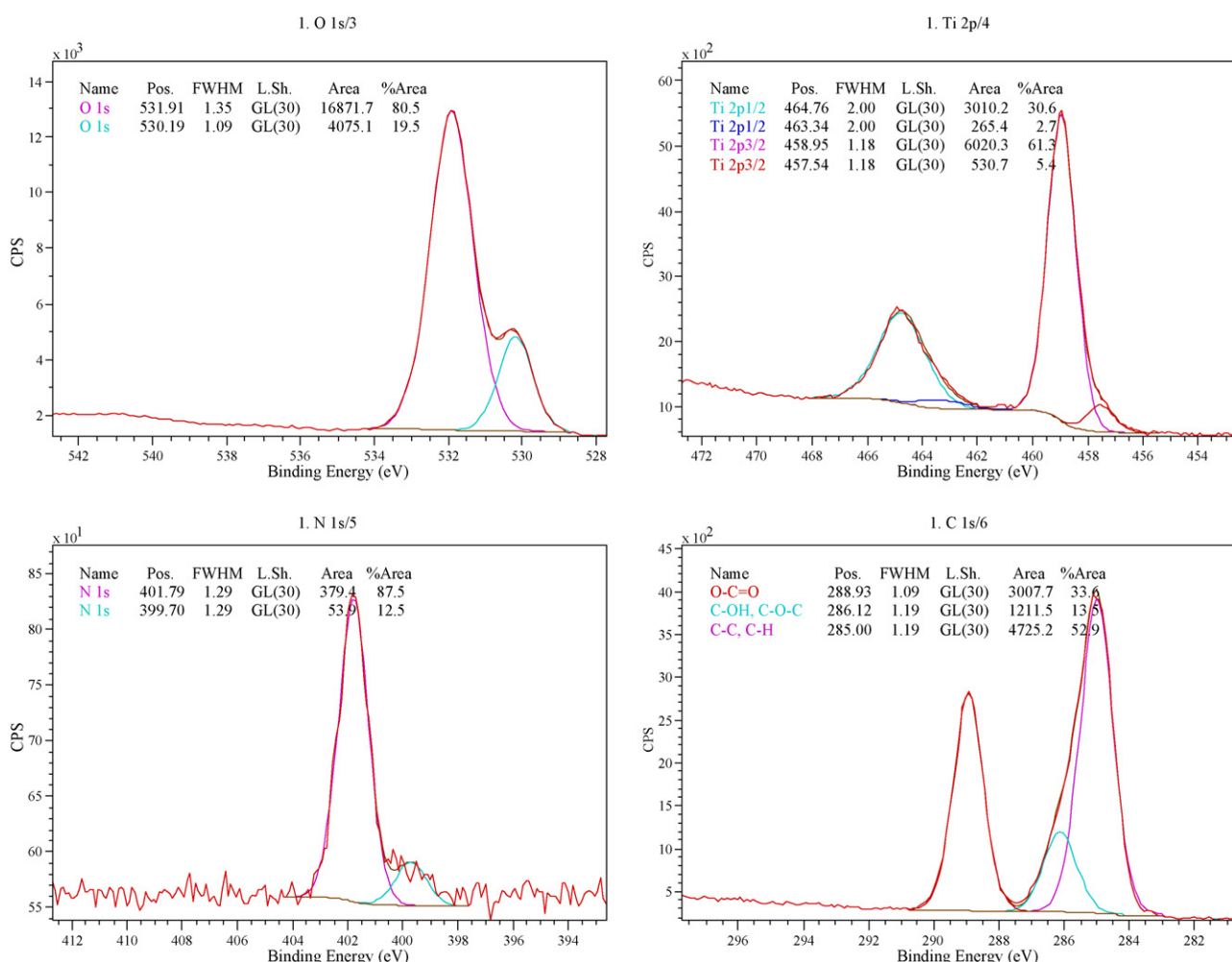
Table 1

Surface area, pore volume, pore diameter, and crystallites size for calcined undoped and doped nanomaterials.

Sample	Surface A (m ² /g)	Pore V (cm ³ /g)	Pore diameter (nm)	Crystal size (nm) ± 1 nm	Crystal structure
TiO ₂	56	0.26	18.9	13.8	A
TiO ₂ -N1	78	0.31	13.7	12.9	A
TiO ₂ -N2	65	0.19	12.0	8.7	A
Zr-TiO ₂	81	0.27	13.7	12.3	A
Zr-TiO ₂ -N1	94	0.25	10.3	11.1	A
Zr-TiO ₂ -N2	72	0.33	18.4	6.2	A

**Fig. 7.** Typical XPS spectrum for Zr modified N-doped TiO₂ as-prepared nanomaterials.

For further analysis of the chemical structure of the investigated samples, five areas of the deconvoluted XPS spectrum for the Zr-TiO₂-N as-prepared nanomaterials were examined: i.e. Ti 2p around 460 eV, Zr 3d around 183 eV, N 1s around 400 eV, O 1s around 530 eV and C 1s around 286 eV region (see Fig. 8). When scanning the Ti 2p and Zr 3d XPS regions, significant differences are observed at the binding energies between the pure TiO₂ and the modified system. According to Galindo et al., TiO₂ Ti 2p_{3/2} and ZrO₂ Zr 3d_{5/2} showed peaks at the binding energies 458.8 and 183 eV, respectively [34]. It was observed previously that introducing Zr metal ion into the lattice shifts the binding energy [21]. This XPS analysis revealed that regardless of Zr modification, the binding energy for Ti 2p_{3/2} shifted to lower values compared to pure TiO₂. The small shift of binding energy of the Ti 2p_{3/2} peak is attributed to the change of the valence state of Ti₄⁺. This supports that upon doping, Ti₄⁺ is converted to Ti₃⁺. The observed binding energy of zirconia Zr 3d_{5/2}, also shows a lower value compared to pure zirconia.

**Fig. 8.** Deconvoluted XPS spectrum for (A) O, (B) Ti, (C) N, and (D) in N-doped TiO₂ as-prepared nanomaterials.

nia, i.e. 182.70 ± 0.02 . The O 1s XPS spectra also shows significant changes upon N incorporation, with the peak shifted to a lower binding energy, i.e. 529.92 eV compared to the pure oxygen peak in TiO_2 , i.e. 530 eV.

The most interesting changes occur around the C 1s peak, and the resolved C peak shows that three different types of carbon containing groups are present around 288, 286, and 284 eV, representing the O=C=O, C–N, and C–C and C–H groups, respectively. However, only two instead of three carbon groups such as O=C=O, and C–C and C–H were present in the pure TiO_2 system. This additional carbon peak indicates that the amine group is directly absorbed onto the surface of the materials, forming metal complexes. It is well known that with two nonbonding electron, nitrogen acts as a Lewis base and forms complexes with electrophilic metal ions [35].

The analysis of the binding energy of N 1s for the N-doped materials shows that two types of N are present in the as-prepared nanomaterials. An intense peak centered at 401.8 and a small peak centered at 399.9 eV, are assigned to chemisorbed and interstitial N, respectively [36–39]. However, the binding energies are greater than the typical binding energy of 397.2 eV in TiN [40]. This higher energy shift can be attributed to the 1s electron binding energy of the N atom in the environment of O–Ti–N. When nitrogen substitutes for the oxygen in the initial O–Ti–O structure, the electron density around N is reduced, compared to that in a TiN crystal, because of the O atom bonded to the Ti atom [36]. After heat treatment, there is only one peak which is centered at 400 eV. Recently, most of the studies regarding the N-doped TiO_2 systems have performed XPS analysis to investigate the chemical state of N. Chen and Burda found that the signal at 401.3 eV in the synthesized nanoparticles is attributed to O–Ti–N, based on the redox chemistry involved [36]. In another study, Yang et al. reported a binding energy of 400.1 eV which was assigned to hyponitrite at the surface [37]. Thus, the nitrogen state in the doped TiO_2 may vary from case to case. However, very recently Huo et al. reported a peak at 399.6 eV, ascribed to the N species incorporation into the titania matrix [28]. Keeping all this in mind, it can be concluded that all N species during calcination were incorporated into the TiO_2 matrix, and the resultant nanomaterials were described as Zr and N codoped TiO_2 .

3.5. BET analysis

The microstructural properties, i.e. the surface area, pore volume, and pore size distributions of all samples were characterized by nitrogen adsorption studies, which were summarized previously in Table 1. The BET surface areas of the calcined materials given in Table 1 show that the modified samples possess higher surface areas compared to the pure nTiO_2 . However, the materials synthesized with a higher amount of TEA showed a lower surface area. This is expected as the SEM and TEM analysis demonstrated that denser materials were formed using a higher amount of TEA. Fig. 9 shows a typical nitrogen adsorption isotherm for calcined Zr modified N-doped TiO_2 , which exhibits an H3 hysteresis loop, typical for mesoporous materials [41]. The typical pore size distribution is inset in Fig. 9 which shows that most pores are larger than 20 nm, whereas a small number of ca. 4 nm diameter pores are present in the samples. The pore volume for all samples did not follow any clear trend with doping while generally the average pore diameters decreased with increasing N content.

3.6. Photocatalytic performance

Methylene blue was chosen as the model organic compound to evaluate the photoactivity of the prepared TiO_2 based nanomaterials. When the MB dye and TiO_2 catalyst suspension is irradiated

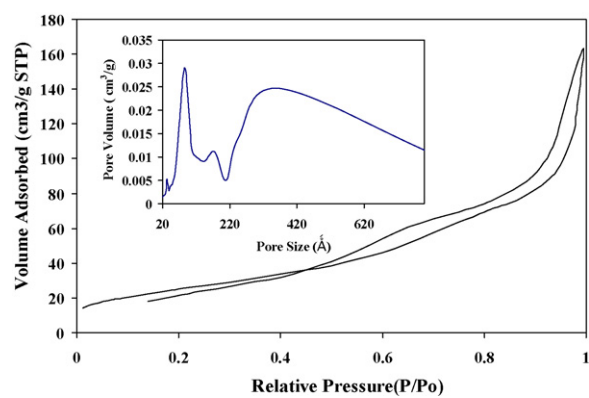


Fig. 9. N_2 adsorption/desorption isotherm of the Zr modified N-doped TiO_2 calcined nanomaterials. Inset shows the pore size distribution.

with the UV radiation, the e^-/h^+ pair is created within the TiO_2 nanocrystallites due to ejection of an electron from the valence band into the conduction band, leaving behind a hole in the valence band (charge-carrier generation). The generated holes may react with the surface-adsorbed OH^- ions forming the $\cdot\text{OH}$ radicals. The $\cdot\text{OH}$ radicals may also be formed by the reaction of dissolved oxygen (O_2) with the generated electrons and the protons forming the hydrogen peroxide (H_2O_2) as an intermediate product, which subsequently gets decomposed to the $\cdot\text{OH}$ radical by releasing the OH^- ion into the aqueous solution. The overall reaction results in the decomposition of the MB dye into carbon dioxide (CO_2), nitrate (NO_3^-) ions, sulfate (SO_4^{2-}) ions, protons, and water. The efficacy of the above mechanism in decomposing the MB dye depends on the effectiveness of the photocatalytic process in transferring the photoinduced e^-/h^+ pair from the particle volume to the particle surface, and subsequently to the surface-adsorbed species. The generated e^-/h^+ pair, hence, must migrate to the particle surface as a separate entity. However, if the TiO_2 nanocrystallite size is relatively larger, the travel distance for the e^-/h^+ pair is increased, facilitating recombination within the particle volume before reaching the particle surface (volume charge-carrier recombination) [42].

Fig. 10 compares the degradation rates for the various synthesized photocatalysts synthesized using scCO₂ for this study. The degradation rate for pure TiO_2 was 0.086 min^{-1} and this value increased with the amount of N in the sample becoming 0.186 and 0.203 min^{-1} for $\text{TiO}_2\text{-N1}$ and $\text{TiO}_2\text{-N2}$ samples, respectively. In the Zr modified system, without N doping the degradation

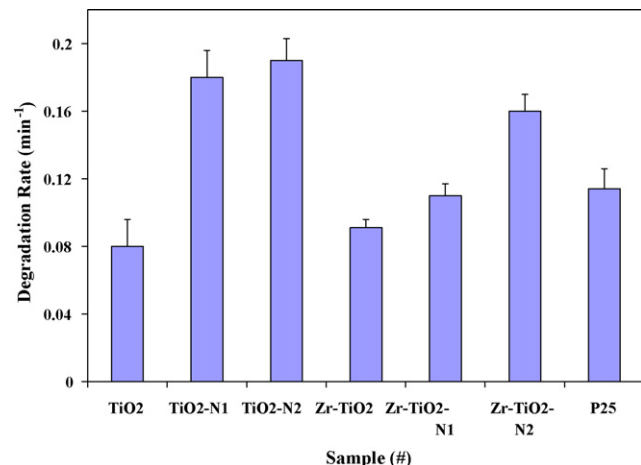


Fig. 10. The variation of the calculated degradation rate for Zr modified N-doped TiO_2 nanomaterials.

rate was 0.092 min^{-1} , whereas the value increased to 0.117 and 0.161 min^{-1} for Zr–TiO₂–N1 and Zr–TiO₂–N2 samples, respectively. The provided results indicate that all N-doped samples show better photocatalytic activity compared to the undoped samples. However, the activity enhancement is higher in TiO₂ samples over Zr modified TiO₂ samples. For comparison purposes, the degradation experiment was also performed using commercially available P25 TiO₂ (surface area $50 \text{ m}^2/\text{g}$), and the calculated value was 0.116 min^{-1} . The degradation rate of N-doped TiO₂ was nearly 1.7 times higher than P-25, showing a good potential for practical applications in photocatalysis.

The enhancement in photocatalytic performance of the N-doped TiO₂ samples can be explained by the higher surface area with mesoporous structure, reduction in the crystallite size and defects induced by N doping [39,43–45]. The higher surface areas with mesoporous structure favor the adsorption of reactant molecules, as well as light absorbance. Moreover, the N-modified samples that were found to consist of smaller crystallites (as determined from the XRD data) provide higher interfacial area and better access to the active sites. In addition, the increase of defects which were observed by the HRTEM images could capture more photoelectrons and thus reduce their recombination with photoinduced holes. These factors could enhance the quantum efficiency, leading to higher photocatalytic activity. In addition, the novel synthesis method utilized eliminated the formation of various secondary and impure phases such as metal titanates and/or metal oxides at high temperatures and inhibited the reduction of the photocatalytic activity of anatase titania [44]. Hence, all N-doped TiO₂ samples prepared using scCO₂ show a higher photocatalytic activity compared to undoped TiO₂ nanomaterials. However, the activity enhancement for Zr modified TiO₂ samples is lower than the unmodified samples, although they had higher surface areas and smaller crystallites. Higher surface areas and smaller crystallites can be advantageous only if favorable surface structures exist in the photocatalyst, facilitating surface transfer of carriers [46]. Future work will further examine the sol–gel reaction pathways and how to control the photocatalyst structure for next-generation reactor geometries.

4. Conclusions

Successful synthesis of ZrO₂ modified N-doped TiO₂ nanomaterials by a simple sol–gel process in scCO₂ demonstrated that this is a promising technique for synthesizing anion- and cation-doped TiO₂ nanostructures. The formed Zr modified TiO₂ nanostructured materials have a high surface area, smaller crystallite size, and greater thermal stability which are highly desirable properties as catalysts, support materials, semiconductors, and electrodes in dye-sensitized solar cells (DSSCs). Moreover, all N-doped systems showed better performance compared to pure TiO₂ nanomaterials and N-doped TiO₂ showed higher activity compared to commercial P25 TiO₂ for MB degradation.

Acknowledgment

The authors thank Nancy Bell from the UWO Nanotechnology Centre for the SEM and Ronald Smith from Biology Department, UWO, for his assistance on TEM. This work was financially sup-

ported by the Canadian Natural Science and Engineering Research Council (NSERC), the Materials and Manufacturing Ontario Emerging Materials program (MMO-EMK), the Canadian Foundation for Innovation (CFI).

References

- [1] A. Kumbhar, G. Chumanov, *J. Nanoparticle Res.* 7 (2005) 489–498.
- [2] C. Chen, X. Li, W. Ma, J. Zhao, H. Hidaka, N. Serpone, *J. Phys. Chem. B* 106 (2002) 318–324.
- [3] N. Arconada, A. Durán, S. Suarez, R. Portela, J. Coronado, B. Sanchez, Y. Castro, *Appl. Catal. B: Environ.* 86 (2009) 1–7.
- [4] L.F. Zhang, H.-B. Fu, Y. Zhu, *Adv. Funct. Mater.* 18 (2008) 2180–2189.
- [5] K. Zhu, N.R. Neale, A. Miedaner, A.J. Frank, *Nano Lett.* 7 (2007) 69–74.
- [6] M.S. Sander, M.J. Côté, W. Gu, B.M. Kile, C.P. Tripp, *Adv. Mater.* 16 (2004) 2052–2057.
- [7] B. Chi, E.S. Victorio, T. Jin, *Nanotechnology* 17 (2006) 2234–2241.
- [8] H. Zhang, G.R. Li, L.P. An, T.Y. Yan, X.P. Gao, H.Y. Zhu, *J. Phys. Chem. C* 111 (2007) 6143–6148.
- [9] R. Asahi, T. Morikawa, T. Ohwaki, K. Aoki, Y. Taga, *Science* 293 (2001) 269.
- [10] C. Burda, Y. Lou, X. Chen, A.C.S. Samia, J. Stout, J.L. Gole, *Nano Lett.* 3 (2003) 1049–1051.
- [11] R. Asahi, T. Morikawa, *Chem. Phys.* 339 (2007) 57–63.
- [12] X. Chen, S.S. Mao, *Chem. Rev.* 107 (2007) 2891–2959.
- [13] X. Wang, J.C. Yu, Y. Chen, L. Wu, X. Fu, *Environ. Sci. Technol.* 40 (2006) 2369–2374.
- [14] B. Ohtani, Y. Ogawa, S.I. Nishimoto, *J. Phys. Chem. B* 101 (1997) 3746–3752.
- [15] M. Pal, J. Garcia-Serrano, P. Santiago, U. Pal, *J. Phys. Chem. C* 111 (2007) 96–102.
- [16] M. Wei, H. Zhou, Y. Konishi, M. Ichihara, H. Sugiha, H. Arakawa, *Inorg. Chem.* 45 (2006) 5684–5690.
- [17] M. Fernandez-Garcia, A. Martinez-Arias, J.C. Hanson, J.A. Rodriguez, *Chem. Rev.* 104 (2004) 4063–4104.
- [18] J.D. Mackenzie, E.P. Bescher, *Acc. Chem. Res.* 40 (2007) 810–818.
- [19] X. Qiu, C. Burda, *Chem. Phys.* 339 (2007) 1–10.
- [20] Y.P. Gao, C.N. Sisk, L.J. Hope-Weeks, *Chem. Mater.* 19 (2007) 6007–6011.
- [21] R.A. Lucky, P.A. Charpentier, *Adv. Mater.* 20 (2008) 1755–1759.
- [22] R. Sui, A.S. Rizkalla, P.A. Charpentier, *Langmuir* 21 (2005) 6150–6153.
- [23] A.H. Romang, J.J. Watkins, *Chem. Rev.* 110 (2010) 459–478.
- [24] R.A. Lucky, R. Sui, J.M.H. Lo, P.A. Charpentier, *Cryst. Growth Des.* (2010), doi:10.1021/cg901145d.
- [25] S.M. Chang, R.A. Doong, *J. Phys. Chem. B* 110 (2006) 20808–20814.
- [26] Y. Cong, J. Zhang, F. Chen, M. Anpo, D. He, *J. Phys. Chem. C* 111 (2007) 10618–10623.
- [27] Z. Zhong, M. Lin, V. Ng, G.X.B. Ng, Y. Foo, A. Gedanken, *Chem. Mater.* 18 (2006) 6031–6036.
- [28] Y. Huo, Z. Bian, X. Zhang, Y. Jin, J. Zhu, H. Li, *J. Phys. Chem. C* (2008).
- [29] C.B. Belver, R. Bellol, A. Fuerte, M. Fernandezgarcia, *Appl. Catal. B: Environ.* 65 (2006) 301–308.
- [30] R.A. Lucky, P.A. Charpentier, *Nanotechnology* 20 (2009) 195601.
- [31] D.J. Reidy, J.D. Holmes, M.A. Morris, *Ceram. Int.* 32 (2006) 235–239.
- [32] Y.-H. Zhang, C.K. Chan, J.F. Porter, W. Guo, *J. Mater. Res. Bull.* 13 (1998) 2602–2609.
- [33] P.P. Lottici, D. Bersani, M. Braghini, A. Montenero, *J. Mater. Sci.* 28 (1993) 177–183.
- [34] I.R. Galindo, T. Viveros, D. Chadwick, *Ind. Eng. Chem. Res.* 46 (2007) 1138–1147.
- [35] C.J. Brinker, G.W. Scherer, *Sol–Gel Science: The Physics and Chemistry of Sol–Gel Processing*, Academic Press, New York, 1990.
- [36] X. Chen, C. Burda, *J. Phys. Chem. B* 108 (2004) 15446–15449.
- [37] J. Yang, H. Bai, X. Tan, J. Lian, *Appl. Surf. Sci.* 253 (2006) 1988–1994.
- [38] O. Diwald, T.L. Thompson, E.G. Goralski, S.D. Walck, J.T. Yates, *J. Phys. Chem. B* 108 (2004) 52–57.
- [39] K.M.N. Parida, B. Naik, *J. Colloid Interface Sci.* 333 (2009) 269–276.
- [40] N.C. Saha, H.G. Tompkins, *J. Appl. Phys.* 72 (1992) 3072.
- [41] S.J. Gregg, K.S.W. Sing, *Adsorption, Surface Area, and Porosity*, 2nd ed., Academic Press, London/Toronto, 1982.
- [42] S.R. Bassaid, D. Robert, M. Chaib, *Appl. Catal. B: Environ.* (2009) 93–97.
- [43] J. Zhu, J. Ren, Y. Huo, Z. Bian, H. Li, *J. Phys. Chem. C* 111 (2007) 18965–18969.
- [44] F.K. Han, V.S.R. Kambala, M. Srinivasan, D. Rajarathnam, R. Naidu, *Appl. Catal. A: Gen.* 359 (2009) 25–40.
- [45] M.M. Joshi, N.K. Labhsetwar, P.A. Mangrulkar, S.N. Tijare, S.P. Kamble, S.S. Rayalu, *Appl. Catal. A: Gen.* 357 (2009) 26–33.
- [46] G.W. Liu, X. Wang, Z. Chen, H. Cheng, G.Q. Lu, *J. Colloid Interface Sci.* 329 (2009) 331–338.